

Floquet Engineering Magnetism and Superconductivity in the Square-Lattice Hubbard Model

Jan-Niklas Herre,^{1,*} Takuya Okugawa,^{2,3} Ammon Fischer,³ Christoph Karrasch,⁴ and Dante M. Kennes^{1,3}

¹*Institute for Theory of Statistical Physics, RWTH Aachen University*

²*Department of Physics, Columbia University, New York, NY 10027, USA*

³*Max Planck Institute for the Structure and Dynamics of Matter,*

Center for Free Electron Laser Science, Luruper Chaussee 149, 22761 Hamburg, Germany

⁴*Technische Universität Braunschweig, Institut für Mathematische Physik,*

Mendelssohnstraße 3, 38106 Braunschweig, Germany

(Dated: February 24, 2026)

We study the interplay of magnetic order and superconductivity in the square-lattice Hubbard model under periodic driving with circularly polarized light. Formulating diagrammatic techniques based on the random-phase approximation in terms of Floquet Green's functions, allows us to analyze fluctuation-driven unconventional pairing for weak-to-moderate interactions. The interplay of repulsive interactions and photo-assisted hopping of electrons gives rise to a rich magnetic phase diagram featuring an antiferromagnetic-to-ferromagnetic transition prior to a Floquet Lifshitz transition. Close to the antiferromagnetic transition, topological $d + id$ -wave superconductivity prevails in the phase diagram for a wide range of drive parameters. At intermediate-to-high frequency driving near the Floquet Lifshitz transition, superconducting orders are tuned from spin-singlet d -wave to spin-triplet p -wave character, providing an effective protocol for Floquet engineering topological superconductivity.

The ability to manipulate quantum materials using tailored laser fields has opened new directions for dynamically controlling their properties [1]. In particular, Floquet engineering—the use of periodic driving to modify the effective low-energy Hamiltonian—has emerged as a promising route to realize exotic nonequilibrium states, ranging from topological phases [2–9] and magnetic order [10–13] to light-induced superconductivity [14–33]. Although many theoretical approaches focus on the high-frequency or low-amplitude limit, where heating is minimal and analytic control is tractable, the low-to-intermediate-frequency regime at arbitrary drive amplitude remains less understood. Recent experiments further demonstrate that Floquet engineering of correlated materials extends beyond Mott insulators [8], underscoring the need for theoretical methods capable of addressing the weak-to-moderate coupling regime under sub-bandwidth driving, with direct relevance to Moiré-based systems [9].

We explore the periodically driven square-lattice Hubbard model, where previous works have investigated the possibility of Floquet engineering magnetic order in the strongly interacting limit [10, 13] and, for weak coupling, suppression of antiferromagnetic (AFM) order at low drive frequencies [34]. In the limit of strong interactions, there has also been progress on the Floquet engineering of chiral d -wave superconductivity [26, 35]. Here, we complement these results using the nonequilibrium Floquet Green's function formalism [36–40] that can be systematically extended into the low- to intermediate-frequency regime beyond the reach of analytical expansions. To assess the emergence of collective charge, spin and superconducting fluctuations, we resort to diagrammatic expansions on the level of the random-phase approximation. This enables us to study the impact of driven fermi-

ology on the formation of electronic order. We find that, in the t - t' Hubbard model away from half-filling driven by circularly polarized light at sub-bandwidth drive frequency, photo-assisted processes lead to a switching between AFM and ferromagnetic (FM) orders. This is fundamentally different from the Floquet Lifshitz transition effects expected in the high-frequency limit, where next-to-nearest neighbor hopping can be tuned to dominate over nearest neighbor hopping. Close to the Floquet engineered magnetic instabilities, we find significant tunability of chiral d/p -wave superconductivity throughout the sub-bandwidth driving regime.

Model. We consider the square-lattice Hubbard model driven by an in-plane electric field and coupled to a metallic reservoir to facilitate a nonequilibrium steady state. The time-dependent Hamiltonian is given by

$$H(t) = - \sum_{ij,\sigma} \tilde{t}_{ij} e^{-i\mathbf{A}(t)\cdot\mathbf{R}_{ij}} \hat{c}_{i\sigma}^\dagger \hat{c}_{j\sigma} + U \sum_i \hat{n}_{i\uparrow} \hat{n}_{i\downarrow} + H_{\text{res}}, \quad (1)$$

where $\hat{c}_{i\sigma}^\dagger$ ($\hat{c}_{i\sigma}$) is the creation (annihilation) operator of a fermion with spin σ on site i and $\hat{n}_{i\sigma} = \hat{c}_{i\sigma}^\dagger \hat{c}_{i\sigma}$. U and \tilde{t}_{ij} are the on-site repulsion and hopping between site i and j , respectively. For the latter, we allow for nearest-neighbor hopping \tilde{t} as well as next-nearest-neighbor hopping \tilde{t}' to break the perfect nesting condition and allow for superconducting order close to the magnetic transition [41]. Circularly polarized light, breaking time-reversal symmetry, is included via Peierls substitution [42] with its vector potential

$$\mathbf{A}(t) = \frac{E_0}{\Omega} (\cos \Omega t, \sin \Omega t), \quad (2)$$

where E_0 is the electrical field strength and Ω the drive frequency (drive period $T = 2\pi/\Omega$). The reservoirs are

modeled by non-interacting tight-binding chains that are weakly coupled via a constant hopping term V to each lattice site independently,

$$H_{\text{res}} = \sum_{\mathbf{k}_r} \varepsilon_{\mathbf{k}_r} \hat{d}_{\mathbf{k}_r}^\dagger \hat{d}_{\mathbf{k}_r} + \sum_{\mathbf{k}\mathbf{k}_r\sigma} V (\hat{c}_{\mathbf{k}\sigma}^\dagger \hat{d}_{\mathbf{k}_r} + \hat{d}_{\mathbf{k}_r}^\dagger \hat{c}_{\mathbf{k}\sigma}). \quad (3)$$

In the wide-band limit [43], this is modeled as a constant hybridization $\gamma = \pi\rho_0|V|^2$ with ρ_0 being the reservoir density of states. The (thermal) reservoir is defined by the reservoir distribution function $f(\omega) = (e^{(\omega-\mu)/T_{\text{res}}} + 1)^{-1}$ at temperature T_{res} and chemical potential μ . The hybridization enters as an imaginary selfenergy through the Dyson equation into the reservoir dressed Green's function of the system.

The system is initially in the uncorrelated normal state (paramagnetic), and we investigate how driving affects collective fluctuations and the emergence of magnetic and superconducting order in the weak-to-moderately interacting regime. The weak coupling to the bath facilitates the formation of a Floquet steady-state that is synchronized with the drive (on the timescale $t^* \sim \gamma^{-1}$) [44]. In this formalism, dissipation and heating balance each other and no other heating channels are available.

High-frequency limit. In the limit of high driving frequency we can gain analytical insight via the Magnus expansion [45], which expands in $1/\Omega$ to find an effectively static Floquet Hamiltonian. The lowest order result for the Hubbard model is known [15, 16, 46, 47], and we can define effective hopping parameters $\tilde{t}_{\text{eff}} \approx \tilde{t}\mathcal{J}_0(E_0/\Omega)$ and $\tilde{t}'_{\text{eff}} \approx \tilde{t}'\mathcal{J}_0(\sqrt{2}E_0/\Omega)$. In this limit, we can find two characteristic points. First, a Floquet Lifshitz transition [48–51] at $E_0/\Omega \approx 2.28$, where $\tilde{t}_{\text{eff}} = \tilde{t}'_{\text{eff}}$, which leads to a topological change in the Fermi surface from a continuous one to separated pockets. Second, close to the Floquet Lifshitz transition lies the dynamical localization point [52], where $\tilde{t}_{\text{eff}} \rightarrow 0$, at $E_0/\Omega \approx 2.4$. Here, the effective model is a square lattice model on an enlarged unit cell with hopping \tilde{t}'_{eff} and tilted by $\pi/4$.

Floquet random phase approximation. Based on the Floquet Green's function formalism [36–40, 53, 54], we start from the retarded non-interacting SU(2)-symmetric Floquet particle-hole susceptibility

$$\begin{aligned} \chi_{nn'}^{\text{ph}}(Q) &= \frac{i}{N} \sum_{l,\mathbf{k}} \int \frac{d\omega}{2\pi} G_{n,n'+l}^{\text{R}}(K) G_{l,0}^{\text{<}}(K-Q) \\ &\quad + G_{n,n'+l}^{\text{<}}(K) G_{l,0}^{\text{A}}(K-Q), \end{aligned} \quad (4)$$

introducing the multi-index $K = (\omega, \mathbf{k})$ for the real frequency ω and the momentum \mathbf{k} as well as discrete Floquet indices n, n', l . The Keldysh Green's functions that fulfill $G_{\mathbf{k}}^X(t, t') = G_{\mathbf{k}}^X(t+T, t'+T)$ for $X \in \{\text{R}, \text{A}, \text{<}\}$ were Fourier transformed twice into

$$G_{K,nn'}^X = \frac{1}{T} \int_0^T d\tilde{t} \int_{-\infty}^{\infty} d\tau e^{i(\omega+n\Omega)t - i(\omega+n'\Omega)t'} G_{\mathbf{k}}^X(t, t'), \quad (5)$$

with $\tilde{t} = \frac{t+t'}{2}$ and $\tau = t - t'$ (see Supplemental Material (SM) for details [55]). Eq. (B5) is a matrix in Floquet space $\hat{\chi}_Q^{\text{ph}}$ and we can define the spin (s) and charge (c) susceptibility as a geometric sum within the random phase approximation

$$\hat{\chi}^{s/c}(Q) = \left[\mathbf{1} \mp \hat{V}_0 \hat{\chi}^{\text{ph}}(Q) \right]^{-1} \hat{\chi}^{\text{ph}}(Q), \quad (6)$$

where the bare (and undriven) interaction is introduced as $\hat{V}_0 = U\mathbf{1}$ with $\mathbf{1}$ the identity matrix. The geometric series of the spin susceptibility diverges at a critical interaction strength $U_c = 1/\lambda_m$ where λ_m is the eigenvalue with maximal real part of all matrices $\hat{\chi}^{\text{ph}}(\mathbf{q}, \omega = 0)$, which is the Stoner criterion for the onset of magnetic order [56]. As long as $U < U_c$, the system remains paramagnetic and subsidiary superconducting order driven by spin-fluctuation exchange [57–61] can arise, captured by the singlet (s) and triplet (t) components of the retarded effective pairing vertex

$$\hat{V}^{\text{P,(s)}}(Q) = \hat{V}_0 + \frac{3}{2} \hat{V}_0^2 \hat{\chi}^{\text{s}}(Q) - \frac{1}{2} \hat{V}_0^2 \hat{\chi}^{\text{c}}(Q), \quad (7)$$

$$\hat{V}^{\text{P,(t)}}(Q) = -\frac{1}{2} \hat{V}_0^2 \hat{\chi}^{\text{s}}(Q) - \frac{1}{2} \hat{V}_0^2 \hat{\chi}^{\text{c}}(Q). \quad (8)$$

Unconventional superconducting order facilitated by nearby magnetic order is analyzed by diagonalizing a linearized gap equation using a static approximation of the vertex $\hat{V}_{\mathbf{k}-\mathbf{k}'}^{\text{P,(s)/(t)}} \equiv \hat{V}^{\text{P,(s)/(t)}}(\mathbf{k}-\mathbf{k}', \omega = 0)$. The superconducting gap equation in the Floquet-Keldysh formalism is given by

$$\Delta_{\mathbf{k};n}^{(\text{s)/(t})} = \frac{i}{N} \sum_{\mathbf{k}';l} V_{\mathbf{k}-\mathbf{k}';n-l}^{\text{P,(s)/(t)}} \int \frac{d\omega'}{2\pi} \mathcal{F}_{\mathbf{k}';l}^{\text{<}}(\omega'). \quad (9)$$

Here, we transformed the Floquet matrices into the single index notation from Ref. [36]. In linear approximation, the anomalous Green's function is obtained as

$$\begin{aligned} \mathcal{F}_{\mathbf{k};nn'}^{\text{<}}(\omega) &= \sum_{lm} G_{\mathbf{k};n,m}^{\text{R}}(\omega) \Delta_{\mathbf{k};m-l}^{(\text{s)/(t})} G_{-\mathbf{k};n',-l}^{\text{>}}(-\omega) \\ &\quad + G_{\mathbf{k};n,m}^{\text{<}}(\omega) \Delta_{\mathbf{k};m-l}^{(\text{s)/(t})} G_{-\mathbf{k};n',-l}^{\text{R}}(-\omega). \end{aligned} \quad (10)$$

With Eq. (B26) we can solve Eq. (B22) as a non-hermitian eigenvalue problem. An eigenvalue $\lambda_{\text{sc}} > 1$ signals the onset of superconducting order, and the corresponding eigenvector contains information about the symmetry of the gap function. Detailed derivations are provided in the SM [55].

In the numerical results, the units are set by the hopping $\tilde{t} = 1$, leading to a bandwidth $W \sim 8$. We choose a small bath hybridization $\gamma = 0.1$, set next-to-nearest neighbor hopping to $\tilde{t}' = -0.2$ and fix the time-averaged filling of the non-interacting (but open and driven) system to $n_f = 0.6$, away from half-filling. This is done through the chemical potential of the reservoir μ , where the reservoir temperature is set to $T_{\text{res}} = 0$. We consider a drive frequency regime within the bandwidth $\Omega \leq W$, from low- ($\Omega = 2.0$) to intermediate- ($\Omega = 5.0$) to high-frequency driving ($\Omega = 8.0$) where photo-assisted processes become relevant.

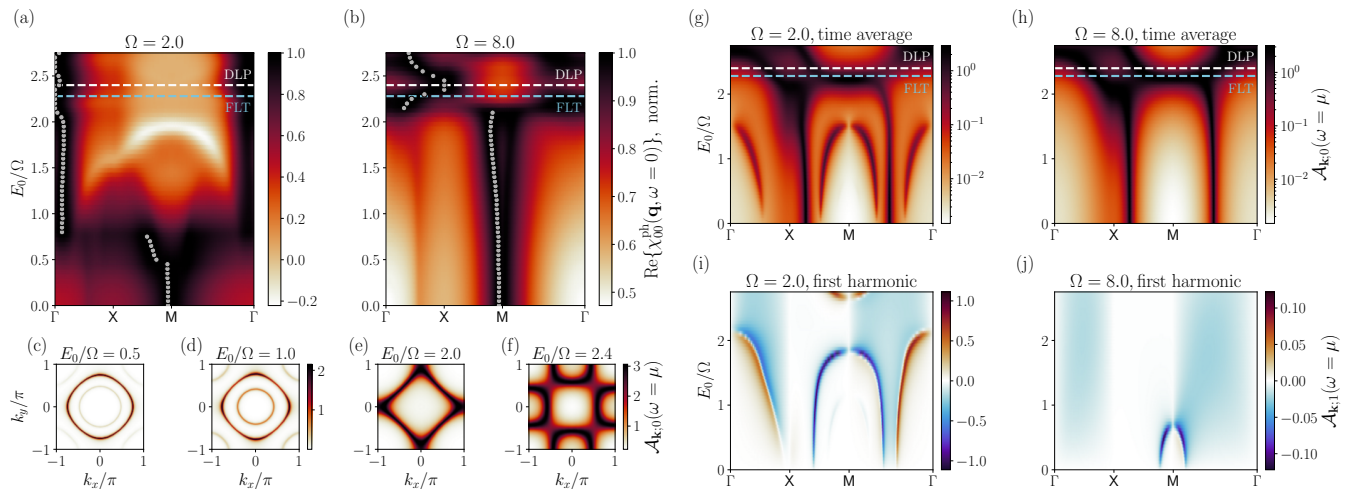


FIG. 1. Time averaged driven non-interacting susceptibility at $\omega = 0$ and spectral function at $\omega = \mu$. Panels (a)-(b): Normalized particle-hole susceptibility in momentum space plotted over drive amplitude. (a) shows low drive frequency, (b) high drive frequency. Gray dots mark the maximum of the susceptibility for a given amplitude. The blue dashed lines mark the Floquet Lifshitz transition (FLT) and the black dashed lines mark the dynamical localization point (DLP). Panels (c), (d) show the Fermi surfaces for $\Omega = 2.0$ at the transition point of the susceptibility maximum. Panels (e), (f) show the same for the high-frequency case ($\Omega = 8.0$, at-bandwidth driving). Panels (g), (h) show the time-averaged spectral function at $\omega = \mu$ in momentum space over drive amplitude for both low and high frequency. Again, the dashed lines mark the Floquet-Lifshitz transition and the dynamical localization point. Panels (i), (j) show the first harmonic ($n = 1$ Floquet component) of the spectral function.

Floquet induced response transition. In Fig. 1, we present the Floquet engineered non-interacting susceptibility and spectral function. For reference, the $t' = 0$ case has been studied in Ref. [39]. For $t' \neq 0$, the periodic drive leads to a Floquet Lifshitz transition of the time-averaged Fermi surface (given by the spectral function $\mathcal{A}_{\mathbf{k};0}(\omega = \mu)$) in the vicinity of the dynamical localization point (Fig. 1(e)-(h)), which also affects the two-particle response function. Figs. 1(a)-(b) show the static ($\omega = 0$) but periodically driven $\Omega \neq 0$) non-interacting susceptibility evaluated along a path connecting the high symmetry points of the Brillouin zone as a function of drive amplitude-to-frequency ratio, E_0/Ω . Panel (b) presents the result for the high-frequency driving, $\Omega = 8.0$ where the effects of the Floquet Lifshitz transition and dynamical localization reflect as a transition of the response peak away from the M -point towards the X -point. Panel (a) shows low-frequency driving, $\Omega = 2.0$. Here, the transition occurs at substantially smaller $E_0/\Omega \sim 0.8$. Before this transition, incommensurate peaks emerge at approximately $E_0/\Omega \sim 0.4$, indicated by a small shift of the peak away from the M -point. This behavior cannot be explained by either the Floquet Lifshitz transition or dynamical localization, as in the $\Omega = 8.0$ case. Instead, one needs to take into account scattering processes not only within the “main” Fermi surface in the time-averaged component (Fig. 1(c)-(d) show no significant change), but also between the Floquet side bands in the time average and higher harmonics that include photo-assisted hoppings and lead to a non-thermal electron occupation; see panels (g)-(j) and Ref. [39]. In this way, additional

overlap of spectral weight with almost zero momentum transfer is generated by the drive, the process only being enabled by the scattering with multiple photons.

Floquet engineering magnetic order. The critical interaction strength U_c , above which the system develops magnetic order, is shown in Fig. 2(a) as a function of E_0/Ω . For the high-frequency case, $\Omega = 8.0$, we observe a monotonic decrease of U_c , whose behavior closely follows the results obtained from a first-order expansion of $\chi_{00}^{\text{ph}}(\mathbf{q} = \mathbf{q}_C, \omega = 0)$, denoted by $\mathcal{O}(E_0/\Omega)$, where \mathbf{q}_C is the momentum giving U_c in the Brillouin zone (see SM for details [55]). This can be interpreted as the peak of the non-interacting susceptibility around the M -point increasing in magnitude as $\tilde{t}_{\text{eff}} \rightarrow 0$ without a change in position, as shown in Fig. 1(b) up to $E_0/\Omega \sim 2$. A further increase of E_0/Ω continues to decrease U_c , despite the change in the peak position induced by the Floquet Lifshitz transition. At the dynamical localization point ($\tilde{t}_{\text{eff}} = 0$), the non-zero values of \tilde{t}'_{eff} and γ prevent U_c from reaching zero. More complex behavior is to be expected in the low-frequency regime, $\Omega = 2.0, 4.0$. We find a suppression of magnetic order that can also be captured by an expansion up to second order, $\mathcal{O}((E_0/\Omega)^2)$, as denoted by the empty dots in Fig. 2(a). This is similar to the results presented in Ref. [34] for the perfect nesting scenario. After the photo-assisted response transition, U_c starts to decrease again and the expansion breaks down. In this regime, the strong band deformation dominates over photo-assisted processes (see Fig. 1(g) at $E_0/\Omega \gtrsim 1.5$), restoring dynamical localization.

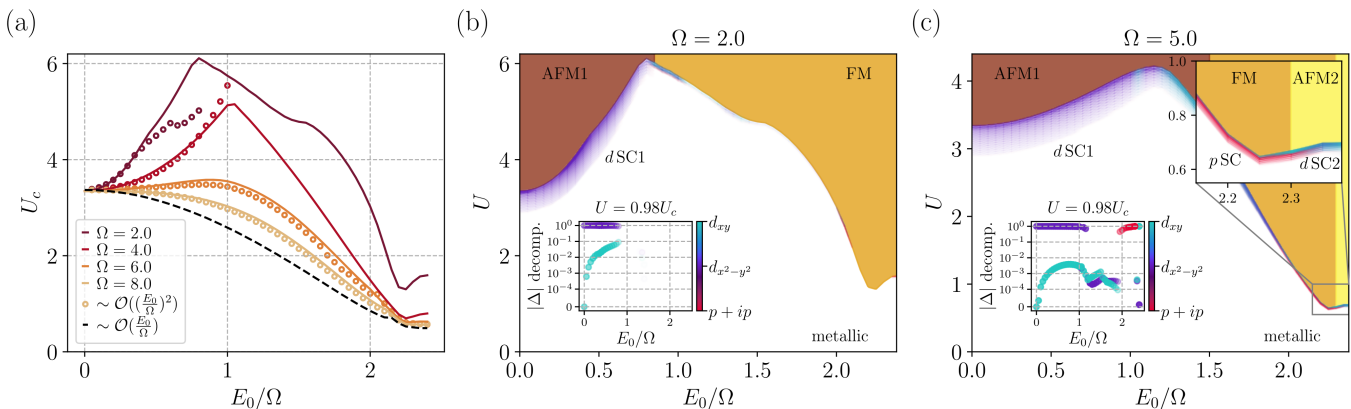


FIG. 2. Interplay of magnetic order and superconductivity in the weak-to-moderate interacting regime. (a) The critical interaction strength for the onset of magnetic order under circularly polarized light as a function of E_0/Ω . Empty dots show results obtained by an expansion of $\chi_{00}^{\text{ph}}(\mathbf{q} = \mathbf{q}_C, \omega = 0)$ up to second order $\mathcal{O}((E_0/\Omega)^2)$ (see SM for details [55]). Dashed line shows the first order expansion ($\mathcal{O}(E_0/\Omega)$) for $\Omega = 8.0$. (b)-(c) Tentative nonequilibrium phase diagram of the time averaged Floquet steady state at low and intermediate-frequency driving. AFM and FM order are identified by the position of the peak of the susceptibility in momentum space. AFM1 is conventional Néel-type AFM order on the square lattice, while AFM2 also entails spin anti-alignment but on the enlarged and tilted lattice given by the next-nearest neighbors (the susceptibility diverges at the X -point), leading to stripe ordering. The superconducting regimes $d\text{SC1}$ and $d\text{SC2}$ correspond to the respective AFM transitions and show different mixing of $d_{x^2-y^2}$ and d_{xy} -symmetry components. Triplet $p + ip$ -wave superconductivity ($p\text{SC}$) is found close to the FM transition at intermediate drive frequency (panel (c)). Insets: Decomposition of the respective symmetry components of the superconducting order.

A nonequilibrium phase diagram of the time-averaged steady state is presented in Figs. 2(b)-(c), revealing the dominant magnetic phases above the critical interaction, U_c (identified in Fig. 2(a)) as well as possible superconducting phases in the vicinity of U_c (see the next section). For both low and intermediate frequencies with $U > U_c$, Néel-type AFM order appears at small E_0/Ω . Upon increasing E_0/Ω , FM order emerges since the peak position of the susceptibility is now located near the Γ -point, as shown in Fig. 1(a). At intermediate-to-high frequencies ($\Omega = 5.0, 8.0$), a stripe AFM ordering develops on the next-to-nearest neighbor bonds, denoted as AFM2 in Fig. 2(c), at the dynamical localization point. At low-frequency driving, photo-assisted processes destroy the AFM2 phase, leaving only the FM phase (Fig. 2(b)).

Superconductivity near the magnetic instability. After establishing the modified magnetic phase diagram of the Floquet-driven Hubbard model, we continue to investigate spin-fluctuation mediated superconductivity. The possible symmetries of the superconducting order parameter are given by the irreducible representations of the C_{4v} point group of the underlying square lattice. In addition to the s -wave, the irreps are given in momentum space by $\Delta_{d_{x^2-y^2}}(\mathbf{k}) = \cos k_x - \cos k_y$, $\Delta_{d_{xy}}(\mathbf{k}) = \sin k_x \sin k_y$ and $\Delta_{p_{x(y)}}(\mathbf{k}) = \sin k_{x(y)}$. By projecting the superconducting gap onto the irreps we can determine the gap symmetry [41]. In Figs. 2(b)-(c), one can find different superconducting regimes in the vicinity of magnetic order for the low- and intermediate-frequency case. In the absence of driving ($E_0/\Omega = 0$), but with coupling to the reservoir, we find spin-fluctuation induced $d_{x^2-y^2}$ pairing, as expected from equilibrium [62–

64]. Upon turning on the drive, the $d_{x^2-y^2}$ ordering persists in the vicinity of Néel-type AFM ordering (AFM1) for both low ($\Omega = 2.0$) and intermediate ($\Omega = 5.0$) frequencies up to $E_0/\Omega \lesssim 1$. Although the dominant pairing symmetry remains $d_{x^2-y^2}$, driving induces a mixing with d_{xy} symmetry components (see inset). To investigate the mixing of the sub-components and their topological properties, we calculate the Berry curvature of the associated Bogoliubov-de-Gennes Hamiltonian using Fukui's method [65]. We find that a topological $d_{x^2-y^2} + id_{xy}$ order with Chern number $C = 2$ is induced by driving in the vicinity of AFM1 for both $\Omega = 2.0, 5.0$. In the low-frequency case (Fig. 2(b)), chiral d -wave superconductivity is suppressed as soon as the magnetic instability switches to FM order. Although triplet superconductivity could be expected to emerge in the vicinity of the FM instability, we do not find this order for the given parameters. However, in the intermediate frequency regime (Fig. 2(c)), triplet $p + ip$ -wave superconductivity can be stabilized around $E_0/\Omega \sim 2$ close to the Floquet Lifshitz transition (see also the inset in Fig. 2(c)). With a further increase of E_0/Ω , the effect of the dynamical localization point becomes evident, where $d_{x^2-y^2} + id_{xy}$ order is stabilized again, but now with the d_{xy} component being dominant ($d\text{SC2}$). This phase appears in the vicinity of the magnetic instability towards the stripe AFM order (AFM2), rather than AFM1. All orders are found to be topologically nontrivial (see SM [55]).

Discussion. We leveraged methodological advances to theoretically describe magnetic order and spin-fluctuation-mediated superconductivity in the circularly driven square-lattice Hubbard model. Introducing the

Floquet random-phase approximation approach we could study the effective pairing vertex and the resulting superconducting gap under sub-bandwidth driving. At low drive frequency, photo-assisted hopping and the resulting non-thermal electron occupation generally suppress magnetic order, whereas, at strong drive amplitude, band deformation can still lead to a dynamical localization effect that enhances magnetic order. However, the Floquet engineered fluctuations change the ordering tendency from AFM to FM order. We then investigated the fate of superconducting order in the vicinity of the magnetic instability, finding that superconductivity can generally survive and is engineered into topological $d+id$ order that is stable over a wide range of drive parameters. While low-frequency driving with high amplitude towards the FM regime destroys any superconducting order, at intermediate-frequency driving, p -wave superconductivity emerges together with a second type of topological $d+id$ -wave ordering in the vicinity of the Floquet Lifshitz transition.

We have shown that analytical expansions cannot be reliably extrapolated from their respective limits, but instead the complex interplay of multi-photon processes and deformed bands needs to be fully accounted for in the weak-to-moderate interacting regime. Further improvements to the method would involve its extension to truncated-unity functional renormalization group [66, 67]

and to treat inelastic scattering processes by including frequency and momentum degrees of freedom simultaneously. Both avenues require further advances in quantum field theory simulations, a promising idea being, for example, tensor cross interpolation [68–70].

Our theoretical simulations highlight novel parameter regimes that are accessible in pulsed experiments [8] in which Floquet engineering allows to control the subtle interplay of magnetic and superconducting order. This offers new pathways for understanding the nature of unconventional superconductivity in cuprates [15], rhombohedral multilayer graphenes [71–73] or moiré materials [74–77].

Acknowledgements. We acknowledge fruitful discussions with Qiyu Liu. J. H. acknowledges funding by the Deutsche Forschungsgemeinschaft (DFG, German Research Foundation) - 508440990 - 531215165 (Research Unit “OPTIMAL”). T. O. acknowledges support from the JSPS Overseas Research Fellowships. Simulations were performed with computing resources granted by RWTH Aachen University under project rwth1749 as well as the HPC system Raven and Viper at the Max Planck Computing and Data Facility.

Data availability. The data supporting the findings of this article are not publicly available. The data are available from the authors upon reasonable request.

* jan.herre@rwth-aachen.de

- [1] A. de la Torre, D. M. Kennes, M. Claassen, S. Gerber, J. W. McIver, and M. A. Sentef, Colloquium: Nonthermal pathways to ultrafast control in quantum materials, *Rev. Mod. Phys.* **93**, 041002 (2021).
- [2] T. Oka and H. Aoki, Photovoltaic hall effect in graphene, *Phys. Rev. B* **79**, 081406 (2009).
- [3] T. Oka and S. Kitamura, Floquet engineering of quantum materials, *Annual Review of Condensed Matter Physics* **10**, 387 (2019).
- [4] S. A. Sato, J. W. McIver, M. Nuske, P. Tang, G. Jotzu, B. Schulte, H. Hübener, U. De Giovannini, L. Mathey, M. A. Sentef, A. Cavalleri, and A. Rubio, Microscopic theory for the light-induced anomalous hall effect in graphene, *Phys. Rev. B* **99**, 214302 (2019).
- [5] G. E. Topp, G. Jotzu, J. W. McIver, L. Xian, A. Rubio, and M. A. Sentef, Topological floquet engineering of twisted bilayer graphene, *Phys. Rev. Res.* **1**, 023031 (2019).
- [6] Y. H. Wang, H. Steinberg, P. Jarillo-Herrero, and N. Gedik, Observation of floquet-bloch states on the surface of a topological insulator, *Science* **342**, 453 (2013).
- [7] G. Usaj, P. M. Perez-Piskunow, L. E. F. Foa Torres, and C. A. Balseiro, Irradiated graphene as a tunable floquet topological insulator, *Phys. Rev. B* **90**, 115423 (2014).
- [8] M. Merboldt, M. Schüler, D. Schmitt, J. P. Bange, W. Bennecke, K. Gadge, K. Pierz, H. W. Schumacher, D. Momeni, D. Steil, S. R. Manmana, M. A. Sentef, M. Reutz, and S. Mathias, Observation of floquet states in graphene, *Nature Physics* **21**, 1093 (2025).
- [9] M. Rodriguez-Vega, M. Vogl, and G. A. Fiete, Low-frequency and moiré-floquet engineering: A review, *Annals of Physics* **435**, 168434 (2021), special issue on Philip W. Anderson.
- [10] J. H. Mentink, K. Balzer, and M. Eckstein, Ultrafast and reversible control of the exchange interaction in mott insulators, *Nature Communications* **6** (2015).
- [11] D. Golez, M. Eckstein, and P. Werner, Multiband nonequilibrium $gw + \text{EDMFT}$ formalism for correlated insulators, *Phys. Rev. B* **100**, 235117 (2019).
- [12] M. Sarkar, Z. Lenarcic, and D. Golez, Floquet engineering of binding in doped and photo-doped mott insulators, *Phys. Rev. Res.* **6**, 033331 (2024).
- [13] V. L. Quito and R. Flint, Polarization as a tuning parameter for floquet engineering: Magnetism in the honeycomb, square, and triangular mott insulators, *Phys. Rev. B* **103**, 134435 (2021).
- [14] M. A. Sentef, A. F. Kemper, A. Georges, and C. Kollath, Theory of light-enhanced phonon-mediated superconductivity, *Phys. Rev. B* **93**, 144506 (2016).
- [15] D. M. Kennes, M. Claassen, M. A. Sentef, and C. Karrasch, Light-induced d -wave superconductivity through floquet-engineered fermi surfaces in cuprates, *Phys. Rev. B* **100**, 075115 (2019).
- [16] D. Kennes, A. de la Torre, A. Ron, D. Hsieh, and A. Millis, Floquet engineering in quantum chains, *Physical Review Letters* **120**, 127601 (2018).
- [17] K. Decker, C. Karrasch, J. Eisert, and D. Kennes, Floquet engineering topological many-body localized systems, *Physical Review Letters* **124**, 190601 (2020).

- [18] Y. Takahashi, H. Miyamoto, K. Kuroki, and T. Kaneko, Floquet engineering of effective pairing interactions in a doped band insulator, *Phys. Rev. B* **111**, 125104 (2025).
- [19] A. Sheikhan and C. Kollath, Dynamically enhanced unconventional superconducting correlations in a hubbard ladder, *Phys. Rev. B* **102**, 035163 (2020).
- [20] O. Hart, G. Goldstein, C. Chamon, and C. Castellano, Steady-state superconductivity in electronic materials with repulsive interactions, *Phys. Rev. B* **100**, 060508 (2019).
- [21] Y. Wang, T. Shi, and C.-C. Chen, Fluctuating nature of light-enhanced d -wave superconductivity: A time-dependent variational non-gaussian exact diagonalization study, *Phys. Rev. X* **11**, 041028 (2021).
- [22] U. Kumar and S.-Z. Lin, Inducing and controlling superconductivity in the hubbard honeycomb model using an electromagnetic drive, *Phys. Rev. B* **103**, 064508 (2021).
- [23] H. Dehghani, M. Hafezi, and P. Ghaemi, Light-induced topological superconductivity via floquet interaction engineering, *Phys. Rev. Res.* **3**, 023039 (2021).
- [24] Z.-Z. Li, C.-H. Lam, and J. Q. You, Floquet engineering of long-range p -wave superconductivity: Beyond the high-frequency limit, *Phys. Rev. B* **96**, 155438 (2017).
- [25] Z. Ning, D.-S. Ma, J. Zeng, D.-H. Xu, and R. Wang, Flexible control of chiral superconductivity in optically driven nodal point superconductors with antiferromagnetism, *Phys. Rev. Lett.* **133**, 246606 (2024).
- [26] A. Sheikhan and C. Kollath, Floquet topological superconductivity induced by chiral many-body interaction, *Communications Physics* **5**, 174 (2022).
- [27] N. Tsuji and H. Aoki, Theory of anderson pseudospin resonance with higgs mode in superconductors, *Phys. Rev. B* **92**, 064508 (2015).
- [28] N. Dasari and M. Eckstein, Transient floquet engineering of superconductivity, *Phys. Rev. B* **98**, 235149 (2018).
- [29] M. A. Sentef, Light-enhanced electron-phonon coupling from nonlinear electron-phonon coupling, *Phys. Rev. B* **95**, 205111 (2017).
- [30] M. Knap, M. Babadi, G. Refael, I. Martin, and E. Demler, Dynamical cooper pairing in nonequilibrium electron-phonon systems, *Phys. Rev. B* **94**, 214504 (2016).
- [31] Y. Murakami, N. Tsuji, M. Eckstein, and P. Werner, Nonequilibrium steady states and transient dynamics of conventional superconductors under phonon driving, *Phys. Rev. B* **96**, 045125 (2017).
- [32] H. P. Ojeda Collado, G. Usaj, C. A. Balseiro, D. H. Zanette, and J. Lorenzana, Emergent parametric resonances and time-crystal phases in driven bardeen-cooper-schrieffer systems, *Phys. Rev. Res.* **3**, L042023 (2021).
- [33] T. Kuhn, B. Sothmann, and J. Cayao, Floquet engineering higgs dynamics in time-periodic superconductors, *Phys. Rev. B* **109**, 134517 (2024).
- [34] N. Walldorf, D. M. Kennes, J. Paaske, and A. J. Millis, The antiferromagnetic phase of the floquet-driven hubbard model, *Phys. Rev. B* **100**, 121110 (2019).
- [35] T. Anan, T. Morimoto, and S. Kitamura, Time-dependent gutzwiller simulation of floquet topological superconductivity, *Communications Physics* **7** (2024).
- [36] N. Tsuji, T. Oka, and H. Aoki, Correlated electron systems periodically driven out of equilibrium: Floquet + DMFT formalism, *Phys. Rev. B* **78**, 235124 (2008).
- [37] J. F. Rentrop, S. G. Jakobs, and V. Meden, Nonequilibrium transport through a josephson quantum dot, *Phys. Rev. B* **89**, 235110 (2014).
- [38] A. K. Eissing, V. Meden, and D. M. Kennes, Functional renormalization group in floquet space, *Phys. Rev. B* **94**, 245116 (2016).
- [39] A. Ono and S. Ishihara, Photocontrol of magnetic structure in an itinerant magnet, *Phys. Rev. B* **98**, 214408 (2018).
- [40] A. Ono and S. Ishihara, Nonequilibrium susceptibility in photoinduced floquet states, *Phys. Rev. B* **100**, 075127 (2019).
- [41] A. T. Rømer, A. Kreisel, I. Eremin, M. A. Malakhov, T. A. Maier, P. J. Hirschfeld, and B. M. Andersen, Pairing symmetry of the one-band hubbard model in the paramagnetic weak-coupling limit: A numerical rpa study, *Phys. Rev. B* **92**, 104505 (2015).
- [42] A. P. Jauho and J. W. Wilkins, Theory of high-electric-field quantum transport for electron-resonant impurity systems, *Phys. Rev. B* **29**, 1919 (1984).
- [43] S. G. Jakobs, M. Pletyukhov, and H. Schoeller, Properties of multi-particle green's and vertex functions within keldysh formalism, *Journal of Physics A: Mathematical and Theoretical* **43**, 103001 (2010).
- [44] N. Tsuji, T. Oka, and H. Aoki, Nonequilibrium steady state of photoexcited correlated electrons in the presence of dissipation, *Phys. Rev. Lett.* **103**, 047403 (2009).
- [45] W. Magnus, On the exponential solution of differential equations for a linear operator, *Communications on Pure and Applied Mathematics* **7**, 649 (1954).
- [46] S. A. Weidinger and M. Knap, Floquet prethermalization and regimes of heating in a periodically driven, interacting quantum system, *Scientific Reports* **7**, 45382 (2017).
- [47] M. H. Kalthoff, D. M. Kennes, and M. A. Sentef, Floquet-engineered light-cone spreading of correlations in a driven quantum chain, *Phys. Rev. B* **100**, 165125 (2019).
- [48] I. V. Iorsh, K. Dini, O. V. Kibis, and I. A. Shelykh, Optically induced lifshitz transition in bilayer graphene, *Phys. Rev. B* **96**, 155432 (2017).
- [49] I. V. Iorsh, D. D. Sedov, S. A. Kolodny, R. E. Sinit'skiy, and O. V. Kibis, Floquet engineering of the lifshitz phase transition in the hubbard model, *Phys. Rev. B* **109**, 035104 (2024).
- [50] P. Mohan, S. Nandy, and A. Taraphder, Interplay of floquet lifshitz transitions and topological phase transitions in bilayer dirac materials, *Physical Review B* **98**, 165406 (2018).
- [51] S. Beaulieu, S. Dong, N. Tancogne-Dejean, M. Dendzik, T. Pincelli, J. Maklar, R. P. Xian, M. A. Sentef, M. Wolf, A. Rubio, L. Rettig, and R. Ernstorfer, Ultrafast dynamical lifshitz transition, *Science Advances* **7**, eabd9275 (2021).
- [52] Y. Kawakami, H. Itoh, K. Yonemitsu, and S. Iwai, Strong light-field effects driven by nearly single-cycle 7 fs light-field in correlated organic conductors, *Journal of Physics B: Atomic, Molecular and Optical Physics* **51**, 174005 (2018).
- [53] G. Floquet, Sur les équations différentielles linéaires à coefficients périodiques, *Annales scientifiques de l'École normale supérieure* **12**, 47 (1883).
- [54] A. Kamenev, *Field Theory of Non-Equilibrium Systems* (Cambridge University Press, 2011).
- [55] Supplemental Material available at [URL] (2025).
- [56] E. C. Stoner, Collective Electron Ferromagnetism, *Proceedings of the Royal Society of London Series A* **165**, 372 (1938).

- [57] N. F. Berk and J. R. Schrieffer, Effect of ferromagnetic spin correlations on superconductivity, *Phys. Rev. Lett.* **17**, 433 (1966).
- [58] N. Bickers and D. Scalapino, Conserving approximations for strongly fluctuating electron systems. i. formalism and calculational approach, *Annals of Physics* **193**, 206 (1989).
- [59] D. J. Scalapino, A common thread: The pairing interaction for unconventional superconductors, *Rev. Mod. Phys.* **84**, 1383 (2012).
- [60] J. Linder and A. V. Balatsky, Odd-frequency superconductivity, *Rev. Mod. Phys.* **91**, 045005 (2019).
- [61] A. Fischer, Designing correlated quantum states in van der Waals heterostructures, PhD thesis, RWTH Aachen University (2025).
- [62] J. R. Schrieffer, X.-G. Wen, and S.-C. Zhang, Spin-bag mechanism of high-temperature superconductivity, *Phys. Rev. Lett.* **60**, 944 (1988).
- [63] J. R. Schrieffer, X. G. Wen, and S. C. Zhang, Dynamic spin fluctuations and the bag mechanism of high- T_c superconductivity, *Phys. Rev. B* **39**, 11663 (1989).
- [64] A. Eberlein and W. Metzner, Superconductivity in the two-dimensional $t-t'$ -hubbard model, *Phys. Rev. B* **89**, 035126 (2014).
- [65] T. Fukui, Y. Hatsugai, and H. Suzuki, Chern numbers in discretized brillouin zone: Efficient method of computing (spin) hall conductances, *Journal of the Physical Society of Japan* **74**, 1674 (2005).
- [66] J. B. Profe and D. M. Kennes, Tu^2 frg: a scalable approach for truncated unity functional renormalization group in generic fermionic models, *The European Physical Journal B* **95** (2022).
- [67] A. Ge, N. Ritz, E. Walter, S. Aguirre, J. von Delft, and F. B. Kugler, Real-frequency quantum field theory applied to the single-impurity anderson model, *Phys. Rev. B* **109**, 115128 (2024).
- [68] H. Shinaoka, M. Wallerberger, Y. Murakami, K. Nogaki, R. Sakurai, P. Werner, and A. Kauch, Multiscale space-time ansatz for correlation functions of quantum systems based on quantics tensor trains, *Physical Review X* **13**, 021015 (2023).
- [69] M. Murray, H. Shinaoka, and P. Werner, Nonequilibrium diagrammatic many-body simulations with quantics tensor trains, *Physical Review B* **109**, 165135 (2024).
- [70] S. Rohshap, M. K. Ritter, H. Shinaoka, J. von Delft, M. Wallerberger, and A. Kauch, Two-particle calculations with quantics tensor trains: Solving the parquet equations, *Physical Review Research* **7**, 023087 (2025).
- [71] H. Zhou, T. Xie, T. Taniguchi, K. Watanabe, and A. F. Young, Superconductivity in rhombohedral trilayer graphene, *Nature* **598**, 434 (2021).
- [72] L. Holleis, C. L. Patterson, Y. Zhang, Y. Vituri, H. M. Yoo, H. Zhou, T. Taniguchi, K. Watanabe, E. Berg, S. Nadj-Perge, *et al.*, Nematicity and orbital depairing in superconducting bernal bilayer graphene, *Nature Physics* **21**, 444–450 (2025).
- [73] T. Han, Z. Lu, Z. Hadjri, L. Shi, Z. Wu, W. Xu, Y. Yao, A. A. Cotten, O. Sharifi Sedeh, H. Weldeyesus, *et al.*, Signatures of chiral superconductivity in rhombohedral graphene, *Nature* **643**, 654 (2025).
- [74] Y. Cao, V. Fatemi, S. Fang, K. Watanabe, T. Taniguchi, E. Kaxiras, and P. Jarillo-Herrero, Unconventional superconductivity in magic-angle graphene superlattices, *Nature* **556**, 43 (2018).
- [75] Y. Xia, Z. Han, K. Watanabe, T. Taniguchi, J. Shan, and K. F. Mak, Superconductivity in twisted bilayer wse2, *Nature* **637**, 833 (2025).
- [76] Y. Guo, J. Pack, J. Swann, L. Holtzman, M. Cothrine, K. Watanabe, T. Taniguchi, D. G. Mandrus, K. Barmak, J. Hone, *et al.*, Superconductivity in 5.0° twisted bilayer WSe2, *Nature* **637**, 839 (2025).
- [77] Y. Xia, Z. Han, J. Zhu, Y. Zhang, P. Knüppel, K. Watanabe, T. Taniguchi, K. F. Mak, and J. Shan, Simulating high-temperature superconductivity in moiré WSe2 (2025), arXiv:2508.02662 [cond-mat.supr-con].

Supplemental Material for “Floquet Engineering Magnetism and Superconductivity in the Square-Lattice Hubbard Model”

Appendix A: Floquet Green’s function formalism

Since the problem is inherently nonequilibrium, we set up Green’s functions on the Keldysh contour [43, 54]

$$G_{\mathbf{k}\sigma}^{\text{R}}(t, t') = -i\theta(t - t') \left\langle \left\{ c_{\mathbf{k}\sigma}(t), c_{\mathbf{k}\sigma}^{\dagger}(t') \right\} \right\rangle, \quad (\text{A1})$$

$$G_{\mathbf{k}\sigma}^{\text{A}}(t, t') = i\theta(t' - t) \left\langle \left\{ c_{\mathbf{k}\sigma}^{\dagger}(t'), c_{\mathbf{k}\sigma}(t) \right\} \right\rangle, \quad (\text{A2})$$

$$G_{\mathbf{k}\sigma}^{<}(t, t') = i \left\langle c_{\mathbf{k}\sigma}^{\dagger}(t') c_{\mathbf{k}\sigma}(t) \right\rangle, \quad (\text{A3})$$

$$G_{\mathbf{k}\sigma}^{>}(t, t') = -i \left\langle c_{\mathbf{k}\sigma}(t) c_{\mathbf{k}\sigma}^{\dagger}(t') \right\rangle, \quad (\text{A4})$$

where we use the Heaviside function $\theta(t)$ and the (anti-) commutators $\{\dots\}$ and $[\dots]$. The expectation value $\langle \dots \rangle$ is taken with respect to the paramagnetic state, which means that the Green’s functions for spin $\sigma = \uparrow, \downarrow$ are identical. The goal is now to exploit the periodicity of the drive to Fourier transform the Green’s functions into frequency space and obtain a time-periodic description of the Floquet steady state, in essence, applying Floquet theory [53] to Green’s functions. The time average of this steady state allows to interpret it as the effective behavior of a system with potentially completely different characteristics compared to equilibrium. The Green’s functions satisfy

$$G(t, t') = G(t + T, t' + T), \quad (\text{A5})$$

where $T = 2\pi/\Omega$ is the drive period. A double Fourier transform allows us to write, following the definition introduced in Refs. [39, 40],

$$G_{nn'}(\omega) = \frac{1}{T} \int_0^T d\bar{t} \int_{-\infty}^{\infty} d\tau e^{i(\omega+n\Omega)t - i(\omega+n'\Omega)t'} G(t, t'), \quad (\text{A6})$$

$$G(t, t') = \sum_{n=-\infty}^{\infty} \int_{-\infty}^{\infty} \frac{d\omega}{2\pi} e^{-in\Omega\bar{t} - i(\omega + \frac{n}{2}\Omega)\tau} G_{n0}(\omega). \quad (\text{A7})$$

Here we defined the central time $\bar{t} = \frac{1}{2}(t + t')$ and the relative time $\tau = t - t'$. The double index is actually a non-physical redundancy, which however has the advantage to allow for matrix operations like inversion and multiplication [36]. Due to the redundancy, the Green’s function needs to be restricted to the “fundamental domain” $F = [-\Omega/2, \Omega/2)$ [37]. Additionally, we can define a “single-index” notation as

$$G_n(\omega) = \frac{1}{T} \int_0^T d\bar{t} \int_{-\infty}^{\infty} d\tau e^{i\omega\tau + in\Omega\bar{t}} G(t, t'), \quad (\text{A8})$$

which allows for easier numerical convolution. We can translate between the two formulations as

$$G_{nn'}(\omega) = G_{n-n'} \left(\omega + \frac{n+n'}{2} \Omega \right), \quad (\text{A9})$$

$$G_n(\omega) = G_{n+n',n'} \left(\omega - \frac{2n+n'}{2} \Omega \right), \quad (\text{A10})$$

where in the second line n' has to be chosen so that it lies in the fundamental domain $(\omega - \frac{2n+n'}{2}\Omega) \in F$. Generally, we will use the version in Eq. (A6) whenever the inversion of Green’s functions is required or we can exploit the Floquet multiplication rule from [36]. We use Eq. (A8) whenever numerical convolution is needed. To make Floquet Green’s functions numerically tractable, the discrete Floquet indices $n, n' \in \mathbb{Z}$ must be truncated to a sufficiently large number n_{max} . The lower the frequency of the drive and the more Fourier coefficients necessary to model the drive protocol, the more Floquet indices need to be retained.

The retarded Floquet Green’s function of the non-interacting system dressed with the reservoir can be written in

terms of the Floquet Hamiltonian and the hybridization self-energies

$$\Sigma_{\text{res};nn'}^{\text{R/A}}(\omega) = \mp i\gamma\delta_{nn'} , \quad (\text{A11})$$

$$\Sigma_{\text{res};nn'}^{<}(\omega) = 2i\gamma f(\omega + n\Omega)\delta_{nn'} , \quad (\text{A12})$$

$$\Sigma_{\text{res};nn'}^{>}(\omega) = -2i\gamma(1 - f(\omega + n\Omega))\delta_{nn'} , \quad (\text{A13})$$

as [36]

$$(G^{\text{R}})_{\mathbf{k};nn'}^{-1}(\omega) = (\omega + n\Omega + i\gamma)\delta_{nn'} - \epsilon_{\mathbf{k};n-n'} , \quad (\text{A14})$$

which is a matrix that can be inverted to obtain $G_{nn'}^{\text{R}}(\omega)$. Here we introduced the reservoir distribution function $f(\omega) = (e^{(\omega-\mu)/T_{\text{res}}} + 1)^{-1}$ at temperature T_{res} and chemical potential μ . We can tune the filling of the system by adjusting the bias through the bath and setting μ . The Fourier components of the noninteracting dispersion are given by

$$\epsilon_{\mathbf{k},n-n'} = \frac{1}{T} \int_0^T dt \epsilon_{\mathbf{k}}(t) e^{i(n-n')\Omega t} . \quad (\text{A15})$$

For the case of circular light implemented via the Peierls substitution we get the Fourier components of the hoppings in real space as

$$\tilde{t}_{ij}^{(n)} = \tilde{t}_{ij} \mathcal{J}_{-n} \left(\frac{E_0 |\mathbf{R}_{ij}|}{\Omega} \right) e^{in\theta_{ij}} , \quad (\text{A16})$$

where \mathcal{J}_n denote Bessel functions of the first kind and $\mathbf{R}_{ij} = |\mathbf{R}_{ij}|(\cos\theta_{ij}, \sin\theta_{ij})$ [35]. The dispersion $\epsilon_n(\mathbf{k})$ follows from Fourier transforming each Floquet component into momentum space.

The other Green's functions follow as

$$G_{nn'}^{\text{A}}(\omega) = (\hat{G}^{\text{R}})_{nn'}^{\dagger}(\omega) , \quad (\text{A17})$$

$$G_{nn'}^{< / >}(\omega) = (\hat{G}^{\text{R}} \hat{\Sigma}_{\text{res}}^{< / >} \hat{G}^{\text{A}})_{nn'}(\omega) , \quad (\text{A18})$$

where hats denote matrices in Floquet space and $(\hat{A}\hat{B})_{mn} \equiv \sum_l A_{ml}B_{ln}$ is conventional matrix multiplication over Floquet indices [36]. The Floquet spectral function is given by $\mathcal{A}_n(\omega) = -\frac{1}{\pi} \Im G_n^{\text{R}}(\omega)$.

Appendix B: Floquet random phase approximation (RPA)

In the following, we provide an alternative but equivalent formulation of the Floquet random phase approximation given in the main text, based on channel decompositions of the nonequilibrium Bethe-Salpeter equations for two-particle correlation functions. This serves to clarify how the fluctuation exchange approximation of the effective pairing vertex remains valid in the Floquet-Keldysh picture. The central components of the Bethe-Salpeter equations are the non-interacting particle-hole and particle-particle susceptibilities

$$\chi_{\mathbf{q}}^{\text{ph};\text{R}}(t, t') = \frac{1}{N} \sum_{\mathbf{k}} \Pi_{\mathbf{k},\mathbf{q}}^{\text{ph};\text{R}}(t, t') , \quad (\text{B1})$$

$$\chi_{\mathbf{q}}^{\text{pp};\text{R}}(t, t') = \frac{1}{N} \sum_{\mathbf{k}} \Pi_{\mathbf{k},\mathbf{q}}^{\text{pp};\text{R}}(t, t') , \quad (\text{B2})$$

where we defined the corresponding pair propagators

$$\Pi_{\mathbf{k},\mathbf{q}}^{\text{ph};\text{R}}(t, t') = iG_{\mathbf{k}}^{\text{R}}(t, t')G_{\mathbf{k}-\mathbf{q}}^{<}(t', t) + iG_{\mathbf{k}}^{<}(t, t')G_{\mathbf{k}-\mathbf{q}}^{\text{A}}(t', t) , \quad (\text{B3})$$

$$\Pi_{\mathbf{k},\mathbf{q}}^{\text{pp};\text{R}}(t, t') = iG_{\mathbf{k}}^{\text{R}}(t, t')G_{-\mathbf{k}+\mathbf{q}}^{>}(t, t') + iG_{\mathbf{k}}^{<}(t, t')G_{-\mathbf{k}+\mathbf{q}}^{\text{R}}(t, t') . \quad (\text{B4})$$

Fourier transforming the susceptibilities using Floquet Green's functions yields [40]

$$\chi_{\mathbf{q};nn'}^{\text{ph};\text{R}}(\omega) = \frac{i}{N} \sum_{\mathbf{k},l} \int_{-\infty}^{\infty} \frac{d\omega'}{2\pi} G_{\mathbf{k};n,n'+l}^{\text{R}}(\omega') G_{\mathbf{k}-\mathbf{q};l,0}^{<}(\omega' - \omega) + G_{\mathbf{k};n,n'+l}^{<}(\omega') G_{\mathbf{k}-\mathbf{q};l,0}^{\text{A}}(\omega' - \omega) , \quad (\text{B5})$$

$$\chi_{\mathbf{q};nn'}^{\text{pp};\text{R}}(\omega) = \frac{i}{N} \sum_{\mathbf{k},l} \int_{-\infty}^{\infty} \frac{d\omega'}{2\pi} G_{\mathbf{k};n,n'+l}^{\text{R}}(\omega') G_{-\mathbf{k}+\mathbf{q};l,0}^{>}(-\omega' + \omega) + G_{\mathbf{k};n,n'+l}^{<}(\omega') G_{-\mathbf{k}+\mathbf{q};l,0}^{\text{R}}(-\omega' + \omega) . \quad (\text{B6})$$

This is again a matrix in Floquet space like the single particle Green's functions. In the equilibrium limit (zero amplitude or zero frequency) one can show that the retarded susceptibilities are equivalent to the equilibrium susceptibility [40]. In the following, we will drop the R label, $\hat{\chi}_{\mathbf{q}}^{\text{ph};\text{R}}(\omega) \equiv \hat{\chi}_{\mathbf{q}}^{\text{ph}}(\omega)$, since we will only ever consider the retarded component explicitly.

The Bethe-Salpeter equations in terms of vertices Γ (two-particle correlation functions with amputated external legs), can be decomposed into three different channels classified by their two-particle reducibility: Particle-particle (P), crossed particle-hole (C) and direct particle-hole (D) channel (on a one-loop level). The full vertex can then be written using projections between the three channels.

$$\Gamma^{1'2'|12}(\omega_1, \mathbf{k}_1; \omega_2, \mathbf{k}_2; \omega_3, \mathbf{k}_3) = \Lambda + P^{-1}[P] + C^{-1}[C] + D^{-1}[D], \quad (\text{B7})$$

where Λ is the irreducible part of the vertex, which is commonly approximated in the Parquet approximation to be the bare vertex. The dependency on four arguments is reduced to three due to (discrete) translation invariance in space and time. The indices $1'2'|12$ are the Keldysh indices which behave exactly like orbital indices, obeying several symmetries, which in the end allows to define R, A, K components of the vertex on the RPA level [43]. The projectors $X^{-1}[\cdot]$ reorder the Keldysh, momentum, and frequency indices into channel-native ordering with one bosonic transfer momentum (frequency) and two fermionic momenta (frequencies):

$$P[\Gamma](Q_p, K_p, K'_p) = \Gamma(Q_p, K_p + K'_p, K'_p - K_p), \quad (\text{B8})$$

$$C[\Gamma](Q_c, K_c, K'_c) = \Gamma(K_c - K'_c, Q_c, K_c + K'_c), \quad (\text{B9})$$

$$D[\Gamma](Q_d, K_d, K'_d) = \Gamma(K_d + K'_d, K_d - K'_d, Q_d), \quad (\text{B10})$$

where we introduced the multi-index $K := (\omega, \mathbf{k})$ and defined the momenta in the corresponding channels as

$$Q_p = K_1, \quad K_p = \frac{1}{2}(K_2 - K_3), \quad K'_p = \frac{1}{2}(K_2 + K_3), \quad (\text{B11})$$

$$Q_c = K_2, \quad K_c = \frac{1}{2}(K_1 - K_3), \quad K'_c = \frac{1}{2}(K_1 + K_3), \quad (\text{B12})$$

$$Q_d = K_3, \quad K_d = \frac{1}{2}(K_1 + K_2), \quad K'_d = \frac{1}{2}(K_1 - K_2). \quad (\text{B13})$$

The projection of the Keldysh indices turns out to be trivial due to the symmetries described in Ref. [43] and is thus not explicitly noted. One finds that the projections still work if one requires periodicity in time for the interaction vertex $\Gamma(t_1, t'_1; t_2, t'_2) = \Gamma(t_1 + T, t'_1 + T; t_2 + T, t'_2 + T)$, however, it requires an additional Floquet index as in the single particle case [37], which again projects trivially between the channels. The full Bethe-Salpeter equations are of course very complicated to solve numerically, and out of scope for anything beyond quantum dots; see a benchmark of parquet and multiloop FRG in that context in Ref. [67]. Instead we follow the random phase approximation and neglect any feedback between the channels by writing fully decoupled equations for each channel, where we additionally neglect all fermionic momenta (frequencies). For clarity, we first present the real-time version of the RPA equations, and then Fourier transform twice to obtain the Floquet steady state counterpart. For each retarded channel $X \in \{\text{P}, \text{C}, \text{D}\}$, it is

$$X_{\mathbf{q}_X}^{\text{RPA}}(t, t') = X[\Gamma^0]_{\mathbf{q}_X}(t, t') + \xi_X \int dt_1 dt_2 X[\Gamma^0]_{\mathbf{q}_X}(t, t_1) \chi_{\mathbf{q}_X}^\xi(t_1, t_2) X_{\mathbf{q}_X}^{\text{RPA}}(t_2, t'), \quad (\text{B14})$$

where $\xi \in \{\text{pp}, \text{ph}\}$ and $\xi_P = 1/2$, $\xi_C = 1$, $\xi_D = -1$ are channel specific prefactors, following notation in Ref. [61]. Here, we additionally used the fact that the Keldysh rotation decouples the equations in Keldysh space just like in the Dyson equation [43]. We denote by $\Gamma^{0;\text{R}}$ the initial (bare) interaction which we generally assume to be time-independent. Restricting ourselves to the Hubbard model, it is $X[\Gamma^{0;\text{R}}]_{\mathbf{q}_X}(t, t') = \delta_{tt'} U \equiv V_0$ in each channel. We can Fourier transform Eq. (B14) enabling us to turn them into matrix equations

$$\hat{X}_{\mathbf{q}_X}^{\text{RPA}}(\omega_X) = \hat{V}_0 + \xi_X \hat{V}_0 \hat{\chi}_{\mathbf{q}_X}^\xi(\omega_X) \hat{X}_{\mathbf{q}_X}^{\text{RPA}}(\omega_X). \quad (\text{B15})$$

The bare interaction is defined as $\hat{V}_0 = V_0 \mathbb{1}$, where $\mathbb{1}$ denotes the identity matrix. The solution to this equation is a geometric series. The RPA expression for the particle-hole channel is

$$\hat{V}_{\mathbf{q}_C}^{\text{C}}(\omega_C) = \left(\left[\mathbb{1} - \hat{V}_0 \hat{\chi}^{\text{ph}} \right]^{-1} \hat{V}_0 \right)_{\mathbf{q}_C}(\omega_C) \quad (\text{B16})$$

$$\hat{\Delta}_{\mathbf{k}}(t_1, t_2) \quad \mathbf{k}, t_1 \rightarrow \leftarrow -\mathbf{k}, t_2 = \mathbf{k}, t_1 \rightarrow \leftarrow -\mathbf{k}, t_2 \quad \Gamma_{\mathbf{q}=0, \mathbf{k}, \mathbf{k}'}^{(4)}(t'_1, t'_2; t_1, t_2)$$

FIG. 3. The linearized gap equation as a general eigenvalue problem. The hat signifies $\hat{\Delta}$ being a matrix in Keldysh indices, while $\Gamma^{(4)} \equiv \Gamma^{1'2'|12}$ is the vertex projected into the pairing channel with all possible Keldysh indices. We only consider zero-momentum Cooper pairs, thus setting $\mathbf{q} = 0$.

The series diverges at a critical interaction strength $U_c = 1/\lambda_m$ where λ_m is the eigenvalue of all matrices $\hat{\chi}_{\mathbf{q}_C}^{\text{ph}}(\omega_C)$ with maximal real part, which is the well known Stoner criterion for the onset of magnetic order. In the following, we always require staying below U_c , i.e., in the paramagnetic phase.

To investigate how spin fluctuations near the magnetic instability might lead to an effective attractive interaction in the pairing channel, we utilize the projection method known from the fluctuation exchange approximation (FLEX) [58, 59]. For interactions $U < U_c$ we can project the RPA expression for the particle-hole channel Eq. (B16) into the pairing channel, explicitly utilizing crossing relations between the C and D-channel

$$\hat{V}_{\mathbf{k}_P, \mathbf{k}'_P}^{\text{P}}(\omega_P, \omega'_P) = \hat{V}_0 + \frac{\hat{V}_0^2 \hat{\chi}_{\mathbf{k}_P + \mathbf{k}'_P}^{\text{ph}}(\omega_P + \omega'_P)}{\mathbb{1} - \hat{V}_0 \hat{\chi}_{\mathbf{k}_P + \mathbf{k}'_P}^{\text{ph}}(\omega_P + \omega'_P)} + \frac{\hat{V}_0^3 \chi_{\mathbf{k}_P - \mathbf{k}'_P}^{\text{ph}}(\omega_P - \omega'_P)^2}{\mathbb{1} - \hat{V}_0^2 \hat{\chi}_{\mathbf{k}_P - \mathbf{k}'_P}^{\text{ph}}(\omega_P - \omega'_P)^2}. \quad (\text{B17})$$

In the second line, we explicitly enforced the SU(2)-symmetric case in the $\{\uparrow\downarrow\uparrow\downarrow\}$ sector, fully removing the implicit spin dependency. To obtain the singlet (triplet) pairing vertex, we (anti)symmetrize the vertex $\hat{V}^{\text{s(t)}, \text{P}} = \hat{V}_{\mathbf{k}_P, \mathbf{k}'_P}^{\text{P}} \pm \hat{V}_{\mathbf{k}_P, -\mathbf{k}'_P}^{\text{P}}$. We can rewrite this to obtain the formulation of the effective pairing vertex in the main text (Eqs. (7), (8)) by enforcing the *SPOT*-symmetry condition [60] and by introducing the RPA spin and charge susceptibilities (Eq. (6) in the main text).

1. Superconducting gap

With an approximation for the effective pairing vertex induced by spin fluctuations at hand we can investigate the corresponding order parameter, which is the superconducting gap. In its most general form, we can write the order parameter as a Keldysh contour integral with the anomalous Green's function

$$\Delta_{\mathbf{k}}^{12}(t_1, t_2) = \frac{i}{N} \sum_{\mathbf{k}'} \int_{t'_1, t'_2} V_{\mathbf{k}, \mathbf{k}'}^{\text{P}; 1'2'|12}(t'_1, t'_2; t_1, t_2) \mathcal{F}_{\mathbf{k}'}^{1'2'}(t'_1, t'_2), \quad (\text{B18})$$

where for the Keldysh indices, a sum over repeated indices is implied. To obtain a description of the superconducting gap in the Floquet steady state, first Fourier transform Eq. (B18) twice with respect to center and relative times. The general version of the vertex that is dependent on four times can be transformed utilizing the definition in Ref. [37], called "single index" notation therein. Using the native frequency definition of the pairing channel and setting the bosonic transfer momentum to zero, we arrive at

$$\Delta_{\mathbf{k}; n}^{12}(\omega) = \frac{i}{N} \sum_{\mathbf{k}'_l} \int \frac{d\omega'}{2\pi} V_{\mathbf{k}, \mathbf{k}'_l}^{\text{P}; 1'2'|12}(-(n+l)\Omega, \omega, \omega') \mathcal{F}_{\mathbf{k}'_l}^{1'2'}(\omega'). \quad (\text{B19})$$

We concentrate on the gap at equal time $t \equiv t_1 = t_2$, ($\omega = 0$), which has only one independent component on the Keldysh contour [43, 67]. It is given in terms of the lesser anomalous Green's function as

$$\Delta_{\mathbf{k}}(t) = \frac{i}{N} \sum_{\mathbf{k}'} V_{\mathbf{k}, \mathbf{k}'}^{\text{P}; \text{R}}(t) \mathcal{F}_{\mathbf{k}'}^{\leq}(t, t), \quad (\text{B20})$$

where, explicitly,

$$\mathcal{F}_{\mathbf{k}}^{\leq}(t, t') = -i \langle \hat{c}_{\mathbf{k}\uparrow}(t') \hat{c}_{-\mathbf{k}\downarrow}(t) \rangle. \quad (\text{B21})$$

Further, we evaluate the vertex at zero frequency (static approximation), which for the single (triplet) gap leads to

$$\Delta_{\mathbf{k};n}^{(s)/(t)} = \frac{i}{N} \sum_{\mathbf{k}'l} V_{\mathbf{k}-\mathbf{k}';n-l}^{\text{P},(s)/(t)} \int \frac{d\omega'}{2\pi} \mathcal{F}_{\mathbf{k}';l}^{<}(\omega'), \quad (\text{B22})$$

using the singlet (triplet) pairing vertex given by Eqs. (7), (8) in the main text. In the considered drive-parameter regime, neglecting the frequency dependence of the vertex remains a reasonable assumption (within the RPA) although finite frequency effects overall are likely to reduce the pairing strength. The real-time version of the order parameter can be recovered as

$$\Delta_{\mathbf{k}}(t) = \sum_n e^{-in\Omega t} \Delta_{\mathbf{k};n}. \quad (\text{B23})$$

2. Linearized anomalous Green's function

Close to the transition temperature T_c we can express the anomalous Green's function through the normal (bare) Green's function as

$$\begin{aligned} \mathcal{F}_{\mathbf{k}}^{<}(t, t') = & \int dt_1 [G_{\mathbf{k}}^R(t, t_1) G_{-\mathbf{k}}^{>}(t', t_1) \\ & + G_{\mathbf{k}}^{<}(t, t_1) G_{-\mathbf{k}}^R(t', t_1)] \Delta_{\mathbf{k}}(t_1), \end{aligned} \quad (\text{B24})$$

where the Keldysh summation follows from the Langreth rules similar to the pair propagators. The diagrammatic form of the general time-dependent linearized gap is shown in Fig. 3. Fourier transforming Eq. (B24) yields in single-index notation

$$\mathcal{F}_{\mathbf{k};n}^{<}(\omega) = \sum_{l,m} [G_{\mathbf{k};n-l-m}^R(\omega + \frac{l+m}{2}\Omega) G_{-\mathbf{k};l}^{>}(-\omega + \frac{n-l}{2}\Omega) + (G^R \leftrightarrow G^{<})] \Delta_{\mathbf{k};m}. \quad (\text{B25})$$

Using the double-index version of the Floquet Green's functions we have

$$\begin{aligned} \mathcal{F}_{\mathbf{k};nn'}^{<}(\omega) = & \sum_{lm} G_{\mathbf{k};n,m}^R(\omega) \Delta_{\mathbf{k};m-l} G_{-\mathbf{k};n',-l}^{>}(-\omega) \\ & + G_{\mathbf{k};n,m}^{<}(\omega) \Delta_{\mathbf{k};m-l} G_{-\mathbf{k};n',-l}^R(-\omega). \end{aligned} \quad (\text{B26})$$

We can plug Eq. (B26) into Eq. (B22) and solve it as a non-Hermitian eigenvalue problem [58, 61]. The onset of superconducting order is signified by the eigenvalue with maximum real part becoming larger than 1. The symmetry of the superconducting order is encoded in the corresponding eigenvector.

3. Bogoliubov-de-Gennes Hamiltonian

Another way to compute the superconducting gap is to extend the formulation of the Hamiltonian to particle-hole (Nambu) space and consider the corresponding Bogoliubov-de-Gennes (BdG) Hamiltonian

$$H_{\mathbf{k}}^{\text{BdG}}(t) = \begin{pmatrix} \epsilon_{\mathbf{k}}(t) & \Delta_{\mathbf{k}}(t) \\ \Delta_{\mathbf{k}}^*(t) & -\epsilon_{-\mathbf{k}}(t) \end{pmatrix}, \quad (\text{B27})$$

for which we can define the Floquet Greens function in Nambu space as

$$[\mathcal{G}^{-1}]_{\mathbf{k};nn'}^R(\omega) = \begin{pmatrix} \mathbf{G}_{\mathbf{k}}^R(\omega) & \mathbf{F}_{\mathbf{k}}^R(\omega) \\ \bar{\mathbf{F}}_{\mathbf{k}}^R(\omega) & \bar{\mathbf{G}}_{\mathbf{k}}^R(\omega) \end{pmatrix}_{nn'}^{-1} \quad (\text{B28})$$

$$= \begin{pmatrix} \omega_{nn'} - \epsilon_{\mathbf{k};n-n'} & -\Delta_{\mathbf{k};n-n'} \\ -\Delta_{\mathbf{k};n-n'}^* & \omega_{nn'} + \epsilon_{-\mathbf{k};n-n'} \end{pmatrix}, \quad (\text{B29})$$

where we introduced $\omega_{nn'} = (\omega + n\Omega + i\gamma)\delta_{nn'}$. We extract the lesser anomalous Greens function from the corresponding matrix element in

$$\mathcal{G}^{<}(\omega) = \frac{1}{2}(\mathcal{G}^A(\omega) - \mathcal{G}^R(\omega) + \mathcal{G}^K(\omega)). \quad (\text{B30})$$

We use the BdG-Hamiltonian to analyze the band structure and compute the Berry curvature and Chern number.

Appendix C: Implementation

The most numerically intensive task is to compute the non-interacting susceptibility in Eq. (B5). For that we need to truncate the infinite Fourier series that builds the Floquet components to a finite amount n_{\max} so that we deal with matrices of size $n_{\max} \times n_{\max}$. To switch from the double to single index index variant (Eqs. (A9), (A10)) we "stitch" the components of the double index Green's function together, which are each only defined on the fundamental domain F . Here, we need to keep in mind that the truncation cuts of the accessible frequency range down to $\sim n_{\max}\Omega/2$. To reduce the required n_{\max} to properly resolve the Green's function over the whole real frequency axis, we extrapolate its tails with an algebraic fit. This is possible since the main contribution of the Floquet replicas is within the bandwidth W . In the $\omega \rightarrow \infty$ limit the Floquet components of the Green's function follow the known algebraic decay $\sim |\omega|^{-\alpha}$. Thus, we only need enough Floquet components (qualitatively $n_{\max} \sim W/\Omega$) to resolve the center region within the band until the algebraic tail dominates and apply extrapolation for large $|\omega|$. In practice, we checked for convergence in n_{\max} with extrapolation applied (a faulty extrapolation would hinder convergence). This leads to a truncation of the Fourier series down to $n_{\max} = 9 - 14$ components, sufficient for drive frequencies $\Omega \gtrsim 2.0$. The frequency integral is solved using an adaptive quadrature routine using the Gauss-Kronrod 21 rule. At $T_{\text{res}} = 0$ it can also be computed analytically with an eigenvalue decomposition of the Floquet Green's functions as we do not feed frequency-dependent self-energies back into the computation and stay at a one-shot level. Having dealt with the Floquet and frequency dependency, the Floquet Green's function also needs to be evaluated over a sufficiently dense momentum grid that can resolve all features of the Fermi surface. The momentum sum can be solved using the convolution theorem, significantly enhancing numerical efficiency. We use a grid with $N_{\mathbf{q},x} = N_{\mathbf{q},y} = 128$ momentum points.

Next, we Eq. (B17) to obtain the effective pairing vertex that is then plugged into Eq. (B22) together with the lesser anomalous Greens function given by Eq. (B26). This can be diagonalized for the eigenvalue with the largest real part with a sparse eigenvalue solver. For the integration of the anomalous Green's function we can employ analytical frequency integration via eigen decomposition together with the convolution theorem over momentum points, as long as we approximate the vertex to be static in frequency space. We implement everything using efficient parallelization schemes on the GPU provided by the JAX Python framework. The code is only memory-bound and runs in ~ 15 minutes on one NVIDIA H100 GPU. Increasing resolution would require a multi-node GPU implementation but is in principle feasible, as well as including the frequency dependency of the vertex and a fully self-consistent FLEX simulation. This is a matter of ongoing work.

Appendix D: Floquet engineering the effective pairing vertex

The drive affects tunes the pairing vertex such that it can either enhance or suppress superconductivity by turning the nearest neighbor or next nearest neighbor components in real space attractive. In Fig. 4 one can see the momentum resolved time-averaged pairing vertex for representative drive parameters. Peaks at the respective high-symmetry points reveal the expected ordering tendencies. Low amplitude driving keeps the peak close to the M -point, which favors AFM ordering and d -wave superconductivity. Intermediate-frequency, high-amplitude driving leads to a peak close to the Γ -point, thus, we expect FM ordering and, close to the Floquet Lifshitz transition (Fig. 4e)), we find spin-triplet p -wave superconductivity to stabilize. In the high-amplitude, high-frequency case, where $t_{\text{eff}} < t'_{\text{eff}}$ the peak moves to the X -point (Fig. 4f)), where one finds AFM order on an enlarged unit cell of the next-to-nearest neighbors. Here, the d -wave superconducting order mainly has d_{xy} symmetry.

To further understand the mechanism that generates the id_{xy} symmetry components, it is insightful to investigate the real space structure of the effective pairing vertex, see Fig. 5. The bonds on which the effective interaction becomes attractive (negative) determine the gap symmetry. For d_{xy} -symmetry, an attractive interaction on the next-nearest neighbor bonds is required. The interaction on the next-nearest neighbor bonds only becomes attractive in the higher order $n = 1$ components of the vertex. Therefore, oscillations in the effective interaction that are induced through the drive give the gap its $d + id$ character. This also explains the suppression of the id_{xy} components, as these higher order terms are suppressed by Ω .

Appendix E: Symmetry of the superconducting phase

The momentum structure of the time-averaged superconducting gap is shown in Fig. 6 for $U = 0.98U_c$ as obtained from the linearized gap equation. The topology of the gap is analyzed by plugging it into the BdG-Hamiltonian in Eq. (B27) and using Fukui's method [65]. In equilibrium, the symmetry of the superconducting order parameter in the square-lattice Hubbard model is known to be $d_{x^2-y^2}$ due to the antiferromagnetic ordering tendency (Fig. 6(a)-(d)). Under driving, due to the time-reversal-symmetry breaking, the gap picks up a non-trivial complex phase that

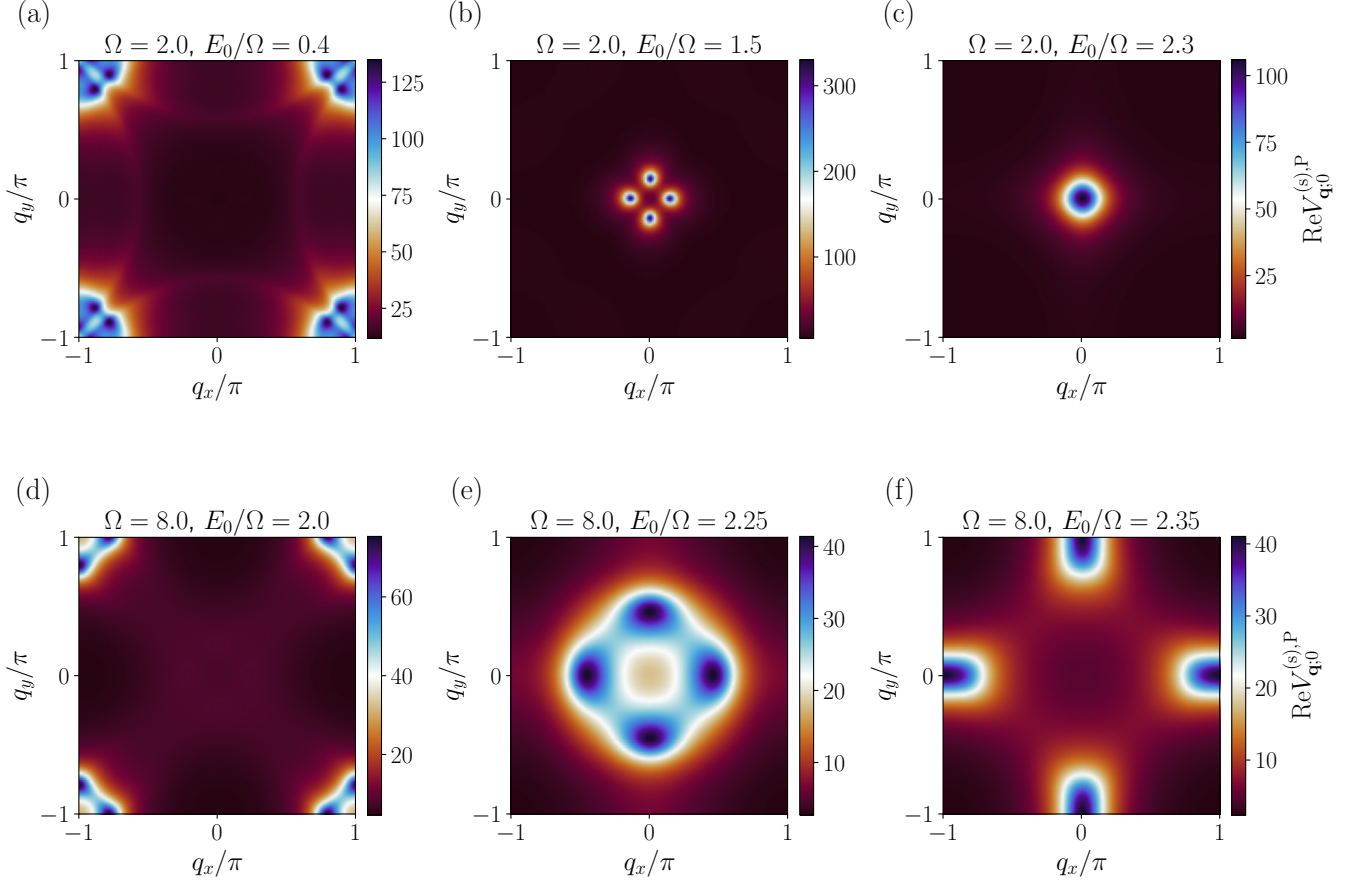


FIG. 4. The time-averaged effective pairing vertex in momentum space (spin-singlet) for representative drive parameters. Panel a) shows a sub-bandwidth drive protocol where the vertex is still peaked close to the M -point, while panels b) and c) show the vertex after the response transition and after the Floquet Lifshitz transition respectively. Panel d) shows the same for high frequency, where the peaks close to the M -point are enhanced. Panel e) shows the vertex close to the Floquet Lifshitz transition. Panel f) shows the vertex close to the dynamical localization point ($t_{\text{eff}}/t'_{\text{eff}} \ll 1$), where the system is effectively an enlarged square lattice tilted by $\pi/4$, thus, the peaks sit at the X -point.

also generally leads to a complex eigenvalue. In the low-amplitude regime this leads to a moderate mixing of id_{xy} symmetry regardless of drive frequency. Effectively, we find chiral $d+id$ -wave superconductivity with a Chern number $C = 2$ in the low-amplitude case, with an increased eigenvalue (Fig. 6(e)-(l)). We thus find agreement with the chiral superconductivity that has been reported in the strongly interacting limit [35]. Additionally, in the intermediate-to-high-frequency case (up to bandwidth W), we find intricate changes in ordering symmetry around the Floquet Lifshitz transition ($\tilde{t}_{\text{eff}}/t'_{\text{eff}} = 1$). Triplet superconducting order is stabilized close to U_c as AFM order is replaced by FM order (Fig. 6(q)-(t)). It has $p_x + ip_y$ symmetry with nontrivial topology ($C = 1$). Beyond the Floquet Lifshitz transition close to the dynamical localization point ($\tilde{t}_{\text{eff}} \rightarrow 0$) this changes into $d + id$ -order again, but now the dominant component is the d_{xy} symmetry (Fig. 6(m)-(p)) with Chern number $C = -2$.

Appendix F: Floquet amplitude expansion

In this section, we describe the derivation of the expansion results presented in Fig. 2(a) of the main text. We found that the qualitative behavior of U_c at intermediate- to high-frequency and low-amplitude driving ($E_0/\Omega < 1$) can be captured using an analytically tractable Floquet cutoff of $n_{\text{max}} = 1$. Furthermore, we found that the overall feature of U_c can be well reproduced by approximating it using the time-averaged components of the particle-hole susceptibility,

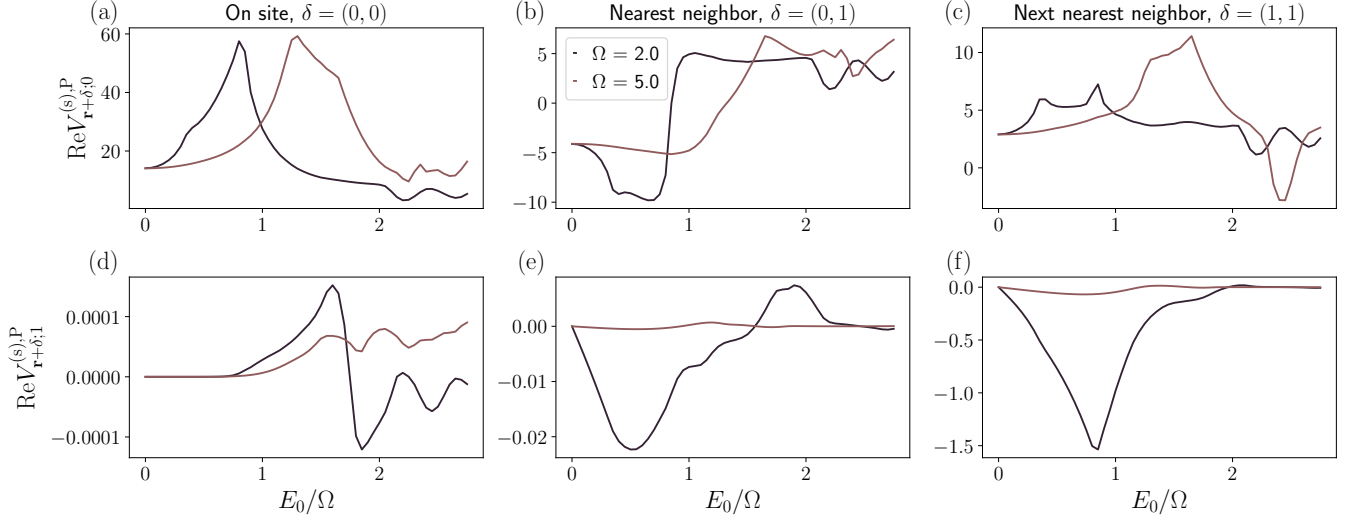


FIG. 5. The real space components of the pairing vertex as a function of drive amplitude for different drive frequencies. The lattice constant is set to $a = 1$. The first row shows the $n = 0$ component, i.e. the time-averaged vertex. The second row shows the $n = 1$ component that describes oscillations of the vertex. (a) and (d) show the onsite interaction which is repulsive. (b) and (e) show the nearest neighbor interaction, which is attractive in the time average, facilitating $d_{x^2-y^2}$ order. (c) and (f) show the next-nearest neighbor interaction that remains repulsive in the time average but becomes attractive in the $n = 1$ component. The magnitude of the $n = 1$ terms is strongly suppressed by Ω .

$$\chi_{\mathbf{q};00}^{\text{ph;R}}(\omega) = \frac{i}{N} \sum_{\mathbf{k},l} \int_{-\infty}^{\infty} \frac{d\omega'}{2\pi} G_{\mathbf{k};0,l}^{\text{R}}(\omega') G_{\mathbf{k}-\mathbf{q};l,0}^{\text{<}}(\omega' - \omega) + G_{\mathbf{k};0,l}^{\text{<}}(\omega') G_{\mathbf{k}-\mathbf{q};l,0}^{\text{A}}(\omega' - \omega), \quad (\text{F1})$$

and evaluating

$$U_c \sim 1/\chi_{\mathbf{q};00}^{\text{ph;R}}(0). \quad (\text{F2})$$

To further simplify the analysis, we approximate $\chi_{\mathbf{q};00}^{\text{ph;R}}(0)$ in the regime of low amplitude. Specifically, we expand $G_{00,\mathbf{k}}^{\text{R/A/<}}$, up to second order of $\epsilon_{\mathbf{k},1}$, which corresponds to the off-diagonal element of Eq. (16) of the main text. This term is approximately proportional to $J_1(\frac{E_0}{\Omega})$ (the next-nearest neighbor hopping term is proportional to $J_1(\frac{\sqrt{2}E_0}{\Omega})$, but since $t \gg t'$, its contribution is much smaller). In the low $\frac{E_0}{\Omega}$ limit, one has $J_0(\frac{E_0}{\Omega}) \gg J_1(\frac{E_0}{\Omega})$. The lowest order contribution corresponds to the Magnus limit, which reproduces the equilibrium results (including reservoir coupling) with the Magnus renormalized hopping amplitude, $t_{\text{eff}} \rightarrow t\mathcal{J}_0(E_0/\Omega)$ and $t'_{\text{eff}} \rightarrow t'\mathcal{J}_0(\sqrt{2}E_0/\Omega)$. The next lowest order (second order) correction is shown in Fig. 2(a) in the main text. Using the following notations,

$$d_{n,\mathbf{k}}(\omega) = (\omega + n\Omega + i\gamma - \epsilon_{\mathbf{k},0})^{-1}, \quad (\text{F3})$$

$$x_{\mathbf{k}} = |\epsilon_{\mathbf{k},1}|^2, \quad (\text{F4})$$

$$R_n(\omega) = 2i\gamma f(\omega + n\Omega), \quad (\text{F5})$$

the expansion up to the second order in $\epsilon_{\mathbf{k},1}$ (i.e., first order in x) is obtained as

$$G_{00}^{\text{R}} \sim d_0 + |\epsilon_{\mathbf{k},1}|^2 d_0 (d_{-1} + d_1) d_0^{-1} \quad (\text{F6})$$

$$G_{00}^{\text{<}} \sim R_0 |d_0|^2 + x \left\{ R_0 2\text{Re} [d_0 d_0^* (d_{-1}^* + d_1^*) d_0^*] + R_{-1} |d_0 d_{-1}|^2 + R_1 |d_0 d_1|^2 \right\}, \quad (\text{F7})$$

where the momentum indices \mathbf{k} and frequency dependence ω have been omitted for brevity. Applying the same procedure to $G_{0\pm 1,\mathbf{k}}^{\text{R/A/<}}$ and $G_{\pm 10,\mathbf{k}}^{\text{R/A/<}}$, i.e. expanding each Green's function up to the second order of $\epsilon_{\mathbf{k},1}$, and performing

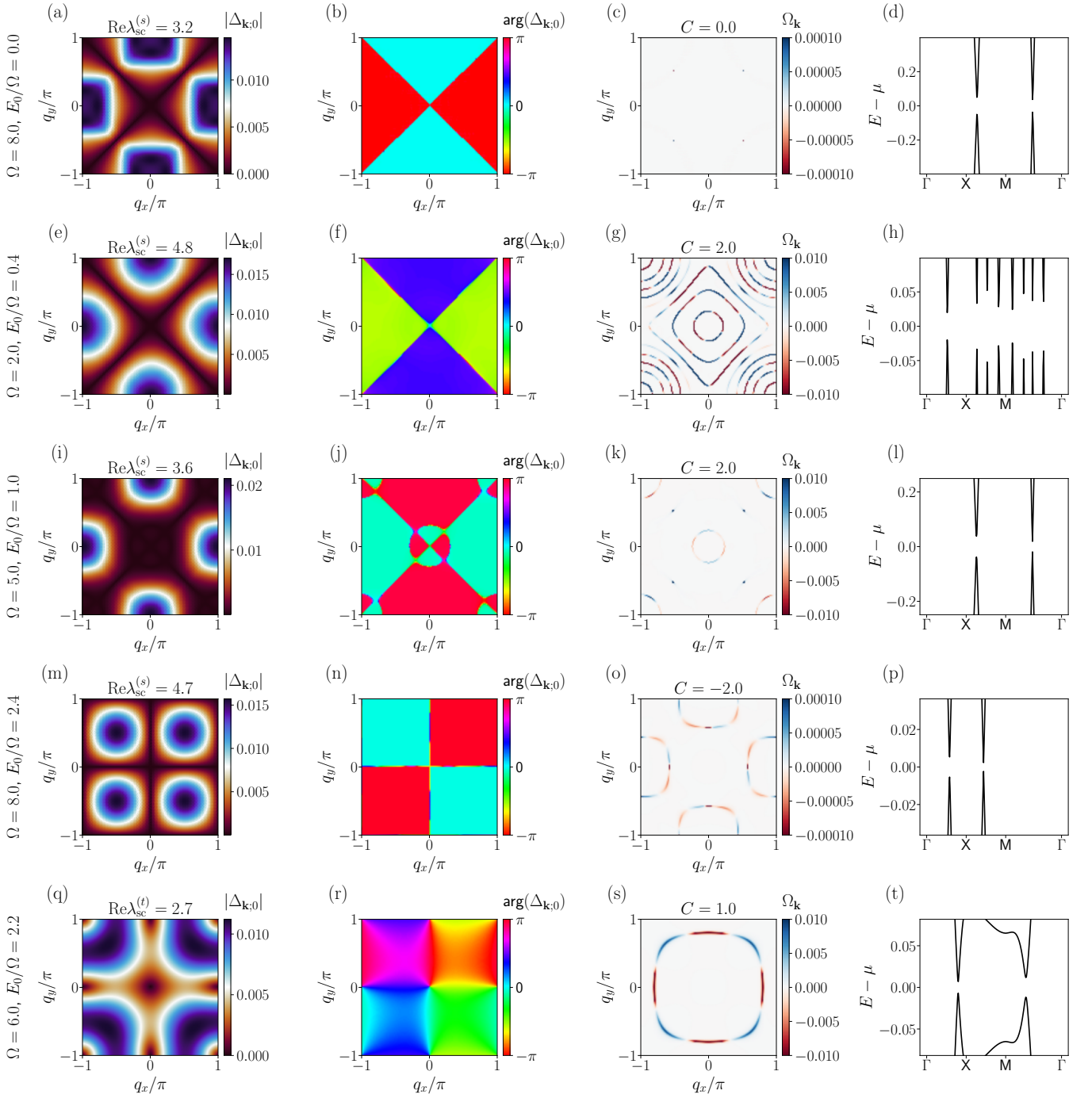


FIG. 6. The time-averaged superconducting singlet/triplet gaps for representative drive parameters. The columns show from left to right: 1) the absolute value of the time-averaged superconducting gap as obtained from the linearized gap equation, together with the real part of the corresponding (largest) eigenvalue, 2) the phase of the superconducting gap, 3) the Berry curvature computed with Fukui's method [65] after plugging the gap into the Floquet BdG-Hamiltonian, 4) the Floquet bands around μ of the gapped BdG model. The rows show from top to bottom: i) the equilibrium case with topologically trivial $d_{x^2-y^2}$ -symmetry ii) low frequency, low amplitude driving with chiral $d + id$ -symmetry, iii) intermediate frequency, low amplitude driving with chiral $d + id$ -symmetry, iv) high frequency (at bandwidth $\Omega = W$), high amplitude driving at the dynamical localization point, showing the second kind of chiral $d + id$ -symmetry with d_{xy} being dominant, v) high frequency, high amplitude driving (just before the Floquet Lifshitz transition) showing chiral spin triplet $p + ip$ -wave superconductivity.

straightforward algebraic manipulations, we obtain $\chi_{\mathbf{q};00}^{\text{ph;R}}(\omega)$ as follows:

$$\chi_{\mathbf{q};00}^{\text{ph;R}}(\omega) = \chi_{\text{mag},\mathbf{q}}^{\text{ph;R}}(\omega) + \delta\chi_{\mathbf{q}}^{\text{ph;R}}(\omega) \quad (\text{F8})$$

$$\begin{aligned} \delta\chi_{\mathbf{q}}^{\text{ph;R}}(\omega) \equiv & \frac{i}{2\pi N} \sum_{\mathbf{k}} \left(\left[|\epsilon_{\mathbf{k},1}|^2 d\chi_{\mathbf{k},\mathbf{q},0}^{\text{ph;R}}(\omega) - |\epsilon_{\mathbf{k}-\mathbf{q},1}|^2 d\chi_{\mathbf{k}-\mathbf{q},\mathbf{q},0}^{\text{ph;R},*}(-\omega) \right] \right. \\ & + \epsilon_{\mathbf{k},1}\epsilon_{\mathbf{k}-\mathbf{q},1} \left[d\chi_{\mathbf{k},\mathbf{q},1}^{\text{ph;R}}(\omega) + d\chi_{\mathbf{k}-\mathbf{q},\mathbf{q},1}^{\text{ph;R},*}(-\omega) \right] \\ & \left. + \epsilon_{\mathbf{k},1}\epsilon_{\mathbf{k}-\mathbf{q},1}^* \left[d\chi_{\mathbf{k},\mathbf{q},2}^{\text{ph;R}}(\omega) + d\chi_{\mathbf{k}-\mathbf{q},\mathbf{q},2}^{\text{ph;R},*}(-\omega) \right] \right) \end{aligned} \quad (\text{F9})$$

$$d\chi_{\mathbf{k},\mathbf{q},n}^{\text{ph;R}}(\omega) \equiv \int d\omega' M_{\mathbf{k}\mathbf{q},n}(\omega', \omega) \quad (\text{F10})$$

$$\begin{aligned} M_{\mathbf{k}\mathbf{q},0}(\omega', \omega) \equiv & \left[R_0(\omega' - \omega) d_{0,\mathbf{k}}(d_{-1,\mathbf{k}} + d_{1,\mathbf{k}}) d_{0,\mathbf{k}} d_{0,\mathbf{k}-\mathbf{q}} d_{0,\mathbf{k}-\mathbf{q}}^* \right. \\ & + R_0(\omega) d_{0,\mathbf{k}}(d_{-1,\mathbf{k}} + d_{1,\mathbf{k}}) d_{0,\mathbf{k}} d_{0,\mathbf{k}}^* d_{0,\mathbf{k}-\mathbf{q}}^* \\ & + R_0(\omega) d_{0,\mathbf{k}} d_{0,\mathbf{k}}^* (d_{-1,\mathbf{k}}^* + d_{1,\mathbf{k}}^*) d_{0,\mathbf{k}}^* d_{0,\mathbf{k}-\mathbf{q}}^* \\ & + R_{-1}(\omega) d_{0,\mathbf{k}}(d_{-1,\mathbf{k}} d_{-1,\mathbf{k}}^*) d_{0,\mathbf{k}}^* d_{0,\mathbf{k}-\mathbf{q}}^* \\ & \left. + R_1(\omega) d_{0,\mathbf{k}}(d_{1,\mathbf{k}} d_{1,\mathbf{k}}^*) d_{0,\mathbf{k}}^* d_{0,\mathbf{k}-\mathbf{q}}^* \right] \end{aligned} \quad (\text{F11})$$

$$\begin{aligned} M_{\mathbf{k}\mathbf{q},1}(\omega', \omega) \equiv & \left[R_{-1}(\omega' - \omega) d_{0,\mathbf{k}} d_{-1,\mathbf{k}} d_{-1,\mathbf{k}-\mathbf{q}} d_{0,\mathbf{k}-\mathbf{q}}^* d_{-1,\mathbf{k}-\mathbf{q}}^* \right. \\ & \left. + R_1(\omega' - \omega) d_{0,\mathbf{k}} d_{1,\mathbf{k}} d_{1,\mathbf{k}-\mathbf{q}} d_{0,\mathbf{k}-\mathbf{q}}^* d_{1,\mathbf{k}-\mathbf{q}}^* \right] \end{aligned} \quad (\text{F12})$$

$$\begin{aligned} M_{\mathbf{k}\mathbf{q},2}(\omega', \omega) \equiv & \left[R_2(\omega' - \omega) d_{0,\mathbf{k}} d_{-1,\mathbf{k}} d_{-1,\mathbf{k}-\mathbf{q}} d_{0,\mathbf{k}-\mathbf{q}} d_{0,\mathbf{k}-\mathbf{q}}^* \right. \\ & \left. + R_2(\omega' - \omega) d_{0,\mathbf{k}} d_{1,\mathbf{k}} d_{1,\mathbf{k}-\mathbf{q}} d_{0,\mathbf{k}-\mathbf{q}} d_{0,\mathbf{k}-\mathbf{q}}^* \right] \end{aligned} \quad (\text{F13})$$

where we suppressed the frequency dependence ω of $d_{n,\mathbf{k}}$ by using implicit notations:

$$d_{n,\mathbf{k}} \rightarrow d_{n,\mathbf{k}}(\omega) \quad (\text{F14})$$

$$d_{n,\mathbf{k}-\mathbf{q}} \rightarrow d_{n,\mathbf{k}-\mathbf{q}}(\omega' - \omega). \quad (\text{F15})$$

In Equation (F8), $\chi_{\text{mag},\mathbf{q}}^{\text{ph;R}}(\omega)$ denotes the contribution of the Magnus limit discussed above, where the hopping amplitudes are renormalized ($t_{\text{eff}} \rightarrow t\mathcal{J}_0(E_0/\Omega)$ and $t'_{\text{eff}} \rightarrow t'\mathcal{J}_0(\sqrt{2}E_0/\Omega)$). This component corresponds to the black line in Fig. 2(a) in the main text (with $\Omega = 8$).

We evaluate Equation (F8) for $\omega = 0$ and $\mathbf{q} = \mathbf{q}_C$, where \mathbf{q}_C is determined from the exact calculation described in the main text. According to our analysis, \mathbf{q}_C can also be accurately obtained from Equation (F8) up to $E_0/\Omega \leq 0.4$ for $\Omega = 2$, $E_0/\Omega \leq 0.8$ for $\Omega = 4$, $E_0/\Omega \leq 2$ for $\Omega = 6$, and $E_0/\Omega \leq 2.2$ for $\Omega = 8$.